Radiomanganese PET Detects Changes in Functional β-Cell Mass in Mouse Models of Diabetes

Reinier Hernandez,[1] Stephen A. Graves,[1] Trillian Gregg,[2,3] Halena R. VanDeusen,[2] Rachel J. Fenske,[2] Haley N. Wienkes,[2] Christopher G. England,[1] Hector F. Valdovinos,[1] Justin J. Jeffery,[4] Todd E. Barnhart,[1] Gregory W. Severin,[5,6] Robert J. Nickles,[1] Michelle E. Kimple,[2,7] Matthew J. Merrins,[2,7,8] and Weibo Cai[1,4,9]

Diabetes 2017;66:2163–2174 | https://doi.org/10.2337/db16-1285

The noninvasive measurement of functional β-cell mass would be clinically valuable for monitoring the progression of type 1 and type 2 diabetes as well as the viability of transplanted insulin-producing cells. Although previous work using MRI has shown promise for functional β-cell mass determination through voltage-dependent Ca^{2+} channel (VDCC)–mediated internalization of Mn^{2+}, the clinical utility of this technique is limited by the cytotoxic levels of the Mn^{2+} contrast agent. Here, we show that positron emission tomography (PET) is advantageous for determining functional β-cell mass using $^{52}Mn^{2+}$ ($t_{1/2}$: 5.6 days). We investigated the whole-body distribution of $^{52}Mn^{2+}$ in healthy adult mice by dynamic and static PET imaging. Pancreatic VDCC uptake of $^{52}Mn^{2+}$ was successfully manipulated pharmacologically in vitro and in vivo using glucose, nifedipine (VDCC blocker), the sulfonylureas tolbutamide and glibenclamide (K_{ATP} channel blockers), and diazoxide (K_{ATP} channel opener). In a mouse model of streptozotocin-induced type 1 diabetes, $^{52}Mn^{2+}$ uptake in the pancreas was distinguished from healthy controls in parallel with classic histological quantification of β-cell mass from pancreatic sections. $^{52}Mn^{2+}$-PET also reported the expected increase in functional β-cell mass in the *ob/ob* model of pretype 2 diabetes, a result corroborated by histological β-cell mass measurements and live-cell imaging of β-cell Ca^{2+} oscillations. These results indicate that $^{52}Mn^{2+}$-PET is a sensitive new tool for the noninvasive assessment of functional β-cell mass.

Type 1 and type 2 diabetes, although arising from different etiologies, are each associated with the functional loss of insulin-secreting β-cells and can lead to life-threatening complications such as cardiovascular disease and neuropathy (1). As such, a variety of therapeutics are being pursued that aim to preserve, expand, or replace β-cells. An imaging modality capable of monitoring functional β-cell mass in vivo as well as the viability of islet- or stem cell–derived β-cell transplants would therefore be invaluable to future therapeutic investigations.

Human pancreatic islets occupy ~4.5% of the pancreas volume and are composed of a mixture of β-, α-, γ-, δ-, and ε-cells (2,3). Because individual islets vary in size from 25 to 400 μm in diameter (3–5) and are nonuniformly distributed throughout the pancreas, quantification is challenging through noninvasive anatomical imaging techniques such as MRI or computed tomography (CT) (6). Alternatively, positron emission tomography (PET) is a technique that involves quantifying the in vivo distribution of a biologically relevant moiety by tracking a positron-emitting radioisotope. Compared with MRI and CT, PET has significantly greater imaging sensitivity and inherently probes

---

[1]Department of Medical Physics, University of Wisconsin-Madison, Madison, WI
[2]Department of Medicine, Division of Endocrinology, Diabetes & Metabolism, University of Wisconsin-Madison, Madison, WI
[3]Program in Biophysics, University of Wisconsin-Madison, Madison, WI
[4]Carbone Cancer Center, University of Wisconsin-Madison, Madison, WI
[5]Center for Nuclear Technologies, Technical University of Denmark, Roskilde, Denmark
[6]Department of Chemistry, Michigan State University, East Lansing, MI
[7]William S. Middleton Memorial Veterans Hospital, Madison, WI
[8]Department of Biomolecular Chemistry, University of Wisconsin-Madison, Madison, WI
[9]Department of Radiology, University of Wisconsin-Madison, Madison, WI

Corresponding authors: Matthew J. Merrins, merrins@wisc.edu, and Weibo Cai, wcai@uwhealth.org.

Received 24 October 2016 and accepted 12 May 2017.

This article contains Supplementary Data online at http://diabetes.diabetesjournals.org/lookup/suppl/doi:10.2337/db16-1285/-/DC1.

R.H. and S.A.G. contributed equally to this work.

physiology rather than anatomy (7), which may prove useful in the clinical quantification of functional β-cell mass.

Mn^{2+}, in a behavior that mimics Ca^{2+}, is freely transported through voltage-dependent Ca^{2+} channels (VDCC) (8,9). Because VDCC activation is required for the release of insulin from β-cells, Mn^{2+} has been proposed as a molecular imaging agent for probing β-cell function and mass using Mn^{2+}-enhanced MRI (10–15). However, this technique is limited by significant cellular toxicity and the slow biological clearance of Mn^{2+}, which prevents the possibility of repeated administration (9,16). Because the sensitivity of PET is several orders of magnitude higher than MRI, the objective of this work was to assess the feasibility of using PET to probe β-cell mass and function.

Herein, we take advantage of the exceptional sensitivity and quantitation capability of PET and the availability of radiomanganese ($^{52}Mn^{2+}$) to noninvasively image functional β-cell mass in vivo. When intravenously (i.v.) injected in mice, $^{52}Mn^{2+}$ ($t_{1/2}$: 5.6 days) showed a rapid accumulation in the mouse pancreas that was sensitive to glucose and pharmacological manipulation of VDCC. We also explored the potential of $^{52}Mn^{2+}$-PET to detect changes in functional β-cell mass in mouse models of type 1 and type 2 diabetes. Overall, our results point to the significant potential for $^{52}Mn^{2+}$ to overcome several limitations of other β-cell imaging agents and potentially become a method of choice for studying β-cell physiology noninvasively.

RESEARCH DESIGN AND METHODS

$^{52}Mn^{2+}$-PET Imaging

Aliquots of the buffered $^{52}Mn^{2+}$ solution (0.01 mol/L NaOAc, pH 6.5) were diluted to the desired injection volume (~200 μL) with PBS, typically 2–4 MBq (~50–100 μCi) per subject. The acquisition of PET images was performed with an Inveon μPET/μCT scanner (Siemens Preclinical Solutions). To study the biodistribution and clearance of $^{52}Mn^{2+}$ in the mouse, 3.7 MBq (100 μCi) of $^{52}Mn^{2+}$ was i.v. injected into female ICR mice. As a result of the long decay half-life of $^{52}Mn^{2+}$ ($t_{1/2}$: 5.6 days), multiple PET scans were recorded between 1 h and 13 days after injection of the radiotracer. Before each scan, mice were anesthetized with isoflurane (4% induction; 1% maintenance) and placed prone in the scanner, and 30–40 × 10^6 coincidence events per mouse static PET scans were acquired (time window, 3.432 ns; energy window, 350−650 keV).

The PET images were reconstructed in Inveon Acquisition Workplace (Siemens Preclinical Solutions) workstation using a nonscatter-corrected three-dimensional ordered subset expectation optimization/maximum a posteriori (OSEM3D/MAP) algorithm. Region-of-interest (ROI) analysis was performed after organs were manually delineated on the PET images. Tissue $^{52}Mn^{2+}$ uptake values are reported as standardized uptake value (SUV), which is normalized to whole-body $^{52}Mn^{2+}$ concentration to account for weight disparities between animal models. The percentage of injected dose per gram of tissue (%ID/g) is also reported in Supplementary Tables 6–9). To acquire dynamic PET scans, mice were anesthetized with isoflurane and the lateral tail vein was catheterized. Simultaneous with the administration of ~1.7 MBq (~50 μCi) of $^{52}Mn^{2+}$ as a fast i.v. bolus, 1-h scans were recorded, and list-mode files were binned into 46 frames (12 × 5 s, 6 × 10 s, 6 × 30 s, 10 × 60 s, 6 × 150 s, 6 × 300 s) and the images reconstructed using the OSEM3D/MAP algorithm. For comparison, 1.7 MBq (50 μCi) $^{52}Mn^{2+}$ was continuously infused with a syringe pump (Model 780100l; KD Scientific) during the first 30 min of a 60-min experiment, and list-mode files were binned into 30 frames (2 min each) and reconstructed using the OSEM3D/MAP algorithm.

Effect of Pharmacological VDCC Manipulation on $^{52}Mn^{2+}$ Uptake In Vivo

Pancreatic $^{52}Mn^{2+}$ uptake was stimulated using glucose and glibenclamide (Tocris Biosciences), which is known to promote insulin release in β-cells via blockade of ATP-sensitive K^+ channels (K_{ATP}). Mice were injected intraperitoneally (i.p.) with 100 μL of 1 g/kg glucose, or glucose plus 5 mg/kg glibenclamide in PBS, 15 min before the i.v. injection of 0.74–1.85 MBq (20 μCi) of $^{52}Mn^{2+}$. VDCC blockade was achieved via i.p. injection of 20 mg/kg nifedipine (MP Biomedicals) dissolved in DMSO. To activate K_{ATP} channels, mice received an i.p. injection of 20 mg/kg diazoxide (Tocris Biosciences) in PBS, a clinically used K_{ATP} agonist, 15 min before injection of 0.74 MBq (20 μCi) of $^{52}Mn^{2+}$. Whole-body PET scans were acquired 1 h after the injection of the radiotracer, after which ex vivo biodistribution analysis was performed.

$^{52}Mn^{2+}$-PET Studies in a Type 1 Diabetes Model

Type 1 diabetes was induced in female ICR mice via one i.p. injection of 180 mg/kg streptozotocin (STZ; MP Biomedical), a toxin that selectively destroys pancreatic β-cells (17). The injectable STZ solution (12.5 mg/mL) was prepared fresh in PBS. The weight of each mouse was measured daily, and blood glucose levels were recorded every other day with a TRUEresult glucometer (Trividia Health Inc.) using blood samples collected from the tail vein. Mice were considered diabetic after two consecutive blood glucose readings above 250 mg/dL and were used for $^{52}Mn^{2+}$-PET imaging studies 1 week after the STZ injection. To evaluate $^{52}Mn^{2+}$ pancreatic uptake in diabetic mice, 0.74 MBq (20 μCi) of radioactivity was administered i.v., and static PET images were recorded 1 h after administration of the tracer. Ex vivo biodistribution was performed after PET acquisition.

$^{52}Mn^{2+}$-PET Studies in a Pretype 2 Diabetes Model

Pancreatic uptake of $^{52}Mn^{2+}$ was measured in 10-week-old wild-type and *ob/ob* mice on the C57BL/6J background. For PET imaging, 0.74 MBq (20 μCi) of $^{52}Mn^{2+}$ was i.v. injected 1 h before PET scan acquisition. Accumulation of $^{52}Mn^{2+}$ in the pancreas and other organs of interest was also quantified by ex vivo biodistribution analysis.

Additional Materials and Methods

Animal studies were conducted under the approval of University of Wisconsin-Madison Institutional Animal

Care and Use Committee. Detailed information on animal models, isotope production, ex vivo biodistribution, islet isolation and imaging, and β-cell mass measurement is provided in the Supplementary Data.

RESULTS

In Vivo Whole-Body PET and Biodistribution of $^{52}Mn^{2+}$ in Normal Mice

The in vivo biodistribution of $^{52}Mn^{2+}$ was investigated noninvasively with PET and ex vivo gamma counting. Figure 1*A* shows coronal planes intersecting the pancreas of ICR mice, in PET scans acquired between 1 h and 13 days after i.v. injection of 3.7 MBq (100 μCi) of $^{52}Mn^{2+}$. A rapid and prominent accumulation of $^{52}Mn^{2+}$ was observed in the pancreas, kidneys, liver, heart, and salivary glands (5.13 ± 0.38, 5.13 ± 0.02, 3.27 ± 0.36, 2.11 ± 0.20, and 2.30 ± 0.26 SUV at 1 h postinjection, respectively; $n = 3$) (Fig. 1*B*). In the subsequent time points during the longitudinal study, $^{52}Mn^{2+}$ uptake gradually declined in all organs except the salivary gland, where uptake remained stable at an SUV of ~3 (Fig. 1*B* and Supplementary Table 1). Uptake of $^{52}Mn^{2+}$ in the pancreas, which was highest at 1 h postinjection, was notably higher than that in the liver and kidneys at all time points. Such favorable pancreas-to-normal organ contrast ratios, which peaked at ~3 days after $^{52}Mn^{2+}$ administration, facilitated an easy delineation of the pancreas (Supplementary Fig. 1). Uptake in the muscle was very low and had little variation during the study. Ex vivo biodistribution was performed after the last PET scan 13 days postinjection, confirming a marked accumulation of $^{52}Mn^{2+}$ in the salivary gland, pancreas, kidneys, and to a lesser extent, the heart and liver (Fig. 1*C* and Supplementary Table 2). Other organs, including the brain, lungs, bones, intestines, stomach, and spleen, displayed low $^{52}Mn^{2+}$ uptake, typically less than 0.5 SUV.

Because the whole-body distribution of $^{52}Mn^{2+}$ occurred largely within 1 h after i.v. administration (Fig. 1), a dynamic PET study was designed to investigate the $^{52}Mn^{2+}$ kinetics during this time. Figure 2 shows the time-activity curves (TACs) resulting from ROI analysis of the dynamic PET data corresponding to the pancreas, liver, kidneys, heart, salivary gland, and muscle under two i.v. administration regimens: rapid bolus injection and 30-min continuous infusion. The analysis of the myocardial TAC revealed extremely fast blood extraction kinetics, with a blood circulation half-life of 10.7 ± 3.5 s in mice administered a rapid i.v. $^{52}Mn^{2+}$ bolus. Consequently, $^{52}Mn^{2+}$ uptake was stabilized in the organs of interests within 5 min postinjection.

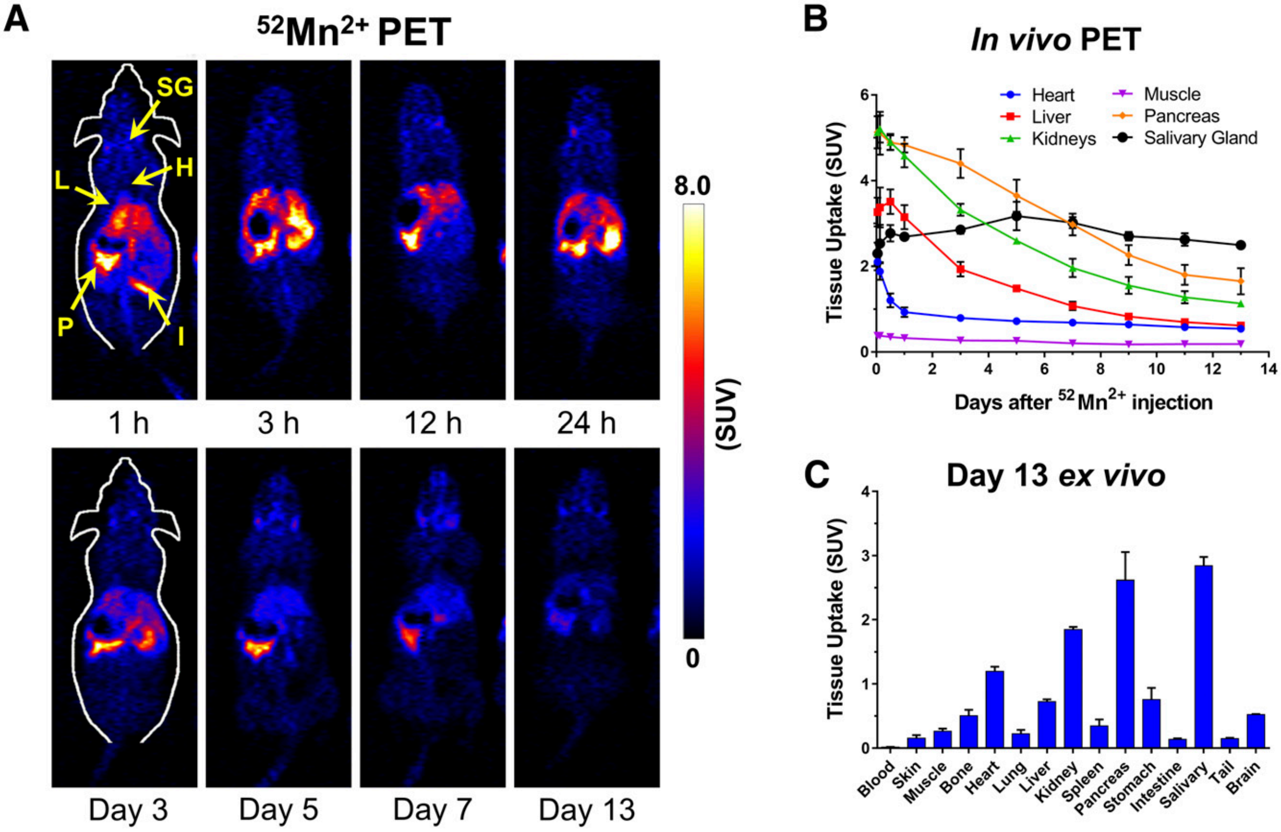

Figure 1—Tissue distribution and pharmacokinetics of $^{52}Mn^{2+}$. *A*: Serial PET images of ICR mice injected i.v. with $^{52}Mn^{2+}$ (no anesthesia except during the PET scans). Coronal PET image slices were selected to best show pancreatic uptake. Arrows point to P, pancreas; H, heart; L, liver; I, intestines; and SG, salivary gland. *B*: ROI-based quantification of $^{52}Mn^{2+}$ uptake in the heart, liver, kidneys, muscle, pancreas, and submandibular salivary gland. *C*: Ex vivo $^{52}Mn^{2+}$ biodistribution of euthanized mice after the last PET scans, determined by gamma counting ($n = 4$).

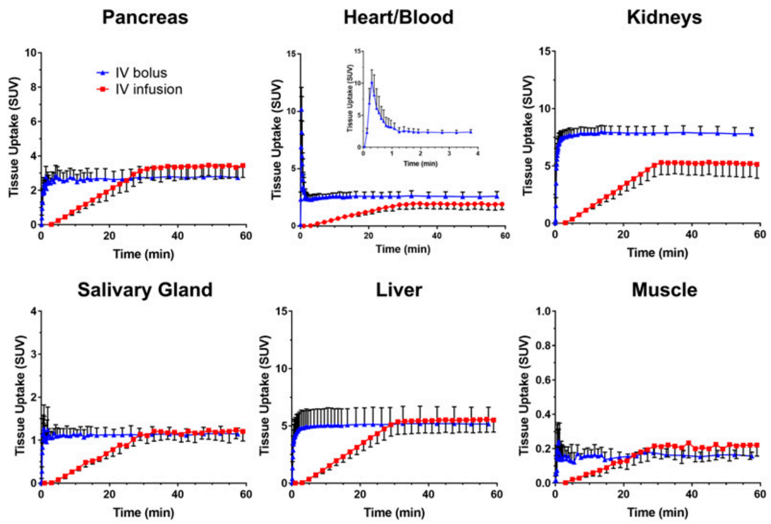

Figure 2—Rapid kinetics of tissue $^{52}Mn^{2+}$ uptake revealed by single i.v. bolus injection or continuous i.v. infusion. Dynamic PET TACs derived from hand-drawn ROIs for the pancreas, heart/blood, liver, kidneys, salivary gland, and muscle. The blue curves indicate TACs in mice injected with a rapid i.v. bolus of $^{52}Mn^{2+}$, and the red curves indicate an i.v. infusion of $^{52}Mn^{2+}$ over the first 30 min of the scans. The inset shows the blood/heart distribution of $^{52}Mn^{2+}$ within the first 4 min after i.v. bolus injection.

A residual radioactivity of 2.60 ± 0.41 SUV was observed in the heart at 1 h postinjection, which was consistent with the specific uptake of Mn^{2+} ions by myocardial tissue. Compared with the static 1 h postinjection PET scans (Fig. 1), similar $^{52}Mn^{2+}$ uptake values were observed after rapid bolus injection in the heart (2.11 ± 0.20 vs. 2.60 ± 0.41 SUV) and muscle (0.38 ± 0.03 vs 0.16 ± 0.02 SUV), whereas the liver (3.27 ± 0.34 vs. 5.16 ± 1.46 SUV) and kidneys (5.13 ± 0.02 vs. 7.81 ± 0.51 SUV) were much higher at the end of the dynamic scan after a rapid i.v. $^{52}Mn^{2+}$ bolus. Interestingly, an ~50% reduction in pancreatic uptake, from 5.13 ± 0.38 to 2.74 ± 0.59 SUV, was observed in the dynamic studies.

As clearly depicted in Fig. 2 (red curves), continuous infusion of $^{52}Mn^{2+}$ over a 30-min period resulted in a linear ramping in organ radioactivity, followed by an immediate plateau upon infusion termination that persisted for the remainder of the experiment. This method highlights the rapid distribution kinetics of $^{52}Mn^{2+}$ and the comparable results obtained by a rapid bolus or continuous infusion of $^{52}Mn^{2+}$. Only the kidney displayed higher radioactivity at 1 h postinjection in mice administered the rapid bolus versus mice receiving the continuous $^{52}Mn^{2+}$ infusion, 7.81 ± 0.51 vs. 5.14 ± 1.21 SUV, respectively ($n = 4$). During the continuous infusion regimen, the pancreas reached an uptake of 3.44 ± 0.69 SUV, which, similar to the rapid bolus injection, was also significantly lower than that in the static PET scans at 1 h postinjection (5.13 ± 0.38 SUV).

Previous reports have shown that many volatile anesthetics, including isoflurane, impair insulin secretion by inhibiting the glucose-dependent inactivation of K_{ATP} channels (18,19). Plausibly, the observed decrease in pancreatic uptake of $^{52}Mn^{2+}$ resulted from mice being anesthetized through the full extent of the studies during the dynamic PET scans. To investigate the effect of isoflurane anesthesia on pancreatic uptake of $^{52}Mn^{2+}$, 1 h postinjection biodistribution experiments were performed under different administration conditions in anesthetized (1% isoflurane) or awake mice. Supplementary Fig. 2 shows that isoflurane significantly inhibited the accumulation of $^{52}Mn^{2+}$ in the pancreas regardless of the administration regimen (rapid bolus vs. infusion) or glucose stimulation, suggesting that isoflurane indeed acts as an indirect VDCC inhibitor upstream of K_{ATP} channel closure.

Uptake of $^{52}Mn^{2+}$ in Isolated Islets

To corroborate the mechanism of $^{52}Mn^{2+}$ uptake in the pancreas and its dependence on VDCC, an ex vivo $^{52}Mn^{2+}$ uptake study was performed in islets isolated from *ob/ob* mice to take advantage of the twofold greater islet yield versus wild-type mice. As a result of the similarities between Mn^{2+} and Ca^{2+} ions, Mn^{2+} uptake by β-cells occurs via influx through VDCC (Fig. 3*A*) (20,21). Isolated islets were incubated with 0.37 MBq (10 μCi) of $^{52}Mn^{2+}$ under several conditions that stimulate/inhibit VDCC (Fig. 3*B*). $^{52}Mn^{2+}$ was readily taken up by islets, even in the presence of low (1 mmol/L) glucose, as expected for the high basal Ca^{2+} and insulin secretion reported for *ob/ob* β-cells (22). $^{52}Mn^{2+}$ uptake was significantly enhanced ($P < 0.05$) when the islets were stimulated with 10 mmol/L glucose. Importantly, $^{52}Mn^{2+}$ uptake was completely blocked by the further application of diazoxide (50 μmol/L), which inhibits the opening of VDCC via activation of K_{ATP} channels. As expected for the clearance of intracellular Ca^{2+} in response to diazoxide (23), intracellular $^{52}Mn^{2+}$ fell below the basal level. Conversely, glucose administered with the K_{ATP} channel blocker tolbutamide (250 μmol/L) resulted in significantly higher $^{52}Mn^{2+}$ retention than glucose alone. Taken together,

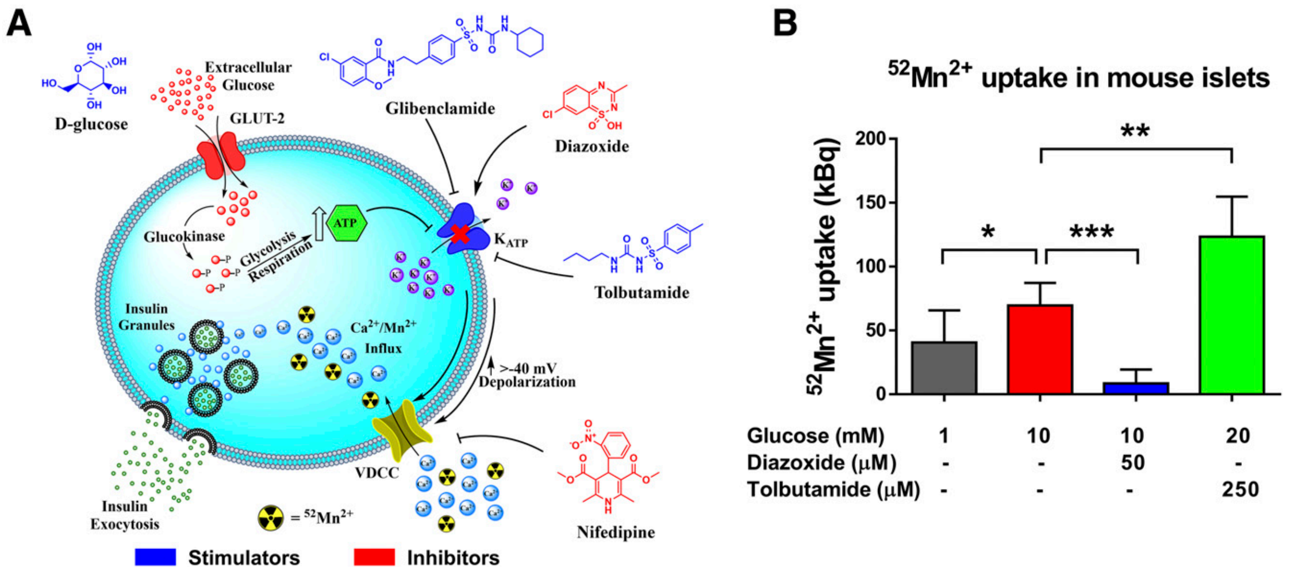

Figure 3—Pharmacological manipulation of VDCC in isolated islets. *A*: Cartoon of the β-cell–triggering pathway. Molecular structures in blue indicate compounds that activate Ca^{2+} influx through VDCC, whereas compounds in red are inhibitory. *B*: Uptake of $^{52}Mn^{2+}$ by isolated *ob/ob* mouse islets. Groups of 50 islets from three preparations were incubated with $^{52}Mn^{2+}$ (370 kBq) in the presence of glucose and VDCC modulators as indicated. Data are presented as mean ± SD. **P* < 0.05; ***P* < 0.01; ****P* < 0.001.

these experiments demonstrate that pancreatic islet uptake of $^{52}Mn^{2+}$ depends on the activity of β-cell VDCC.

Pharmacological Manipulation of $^{52}Mn^{2+}$ Pancreatic Uptake In Vivo

To verify the specificity of $^{52}Mn^{2+}$ accretion in the pancreas noninvasively using PET imaging, $^{52}Mn^{2+}$ pancreatic uptake was pharmacologically manipulated in vivo through the inhibition or stimulation of VDCC. In line with the in vitro results, inhibition of VDCC by direct blockade with nifedipine, or activation of K_{ATP} with diazoxide, resulted in a significant ($P < 0.0001$) abrogation of the PET signal within the pancreas. Figure 4*A* shows coronal PET slices of the pancreas of ICR mice receiving 20 mg/kg i.p. injections of nifedipine or diazoxide 10–15 min before the administration of an i.v. $^{52}Mn^{2+}$ bolus. Compared with the control group, a clear decrease in pancreatic PET signal was observed 1 h after the injection of $^{52}Mn^{2+}$. PET quantification revealed a 44% (5.13 ± 0.36 vs. 2.85 ± 0.92 SUV) and 54% (5.13 ± 0.36 vs. 2.36 ± 0.61 SUV) decline in $^{52}Mn^{2+}$ uptake in groups administered diazoxide and nifedipine, respectively (Fig. 4*B* and *C*). The remnant pancreatic signal suggests that i.p. drug injection resulted in the incomplete blockade of VDCC, or more likely, that some $^{52}Mn^{2+}$ uptake is independent of VDCC (8). However, mice administered glibenclamide (5 mg/kg) exhibited a significant enhancement in pancreatic uptake of $^{52}Mn^{2+}$. The distribution of $^{52}Mn^{2+}$ in other organs of interest, including the heart, liver, kidneys, spleen, and salivary gland, remained largely unaltered among the groups (Supplementary Tables 3 and 4). These results demonstrate the potential of $^{52}Mn^{2+}$ PET imaging to noninvasively detect changes in functional β-cell mass.

$^{52}Mn^{2+}$ Uptake in Mouse Models of Type 1 and Type 2 Diabetes

We further investigated the correlation between pancreatic $^{52}Mn^{2+}$ uptake and functional β-cell mass in a murine model of type 1 diabetes. Diabetes was induced in female ICR mice via a single STZ injection (180 mg/kg). Four days after injection (Fig. 5*A*), mice presented signs of hyperglycemia (blood glucose > 250 mg/dL) and weight loss that indicated a diabetic status. As seen in the PET images (Fig. 5*B*), $^{52}Mn^{2+}$ accumulation within the pancreas of diabetic mice was reduced by ~60%, from 5.13 ± 0.38 SUV (n = 3) in normal mice to 2.04 ± 0.81 SUV (n = 3) in diabetic mice ($P < 0.0001$) (Fig. 5*C*, and Supplementary Tables 3 and 4). Ex vivo biodistribution analysis corroborated a very similar (58%) decrease in pancreatic accumulation of $^{52}Mn^{2+}$ (Fig. 5*D*). To compare $^{52}Mn^{2+}$-PET imaging with a direct histological assessment of β-cell mass, three pancreata per treatment group were weighed, sectioned, and immunostained for insulin. On average, β-cell mass in the STZ-treated mice fell by ~70% compared with the sham-injected ICR mice (Fig. 5*E*), in good agreement with the $^{52}Mn^{2+}$-PET data.

$^{52}Mn^{2+}$-PET imaging studies were also performed in C57BL/6J mice carrying the *lep*^{ob} (*ob/ob*) spontaneous mutation that results in obesity and pretype 2 diabetes. In this case, $^{52}Mn^{2+}$ accumulation in the pancreas of *ob/ob* mice was significantly ($P < 0.001$) higher than in the wild-type C57BL/6J mice (Fig. 6*A*). Pancreatic uptake 1 h after administration of $^{52}Mn^{2+}$ (n = 3) was 4.89 ± 0.68 SUV in wild-type C57BL/6J mice and 7.27 ± 1.03 SUV in *ob/ob* mice (Fig. 6*B*). Ex vivo biodistribution analysis corroborated the statistically significant differences in pancreatic SUV between the groups ($P < 0.001$) (Supplementary Fig. 3

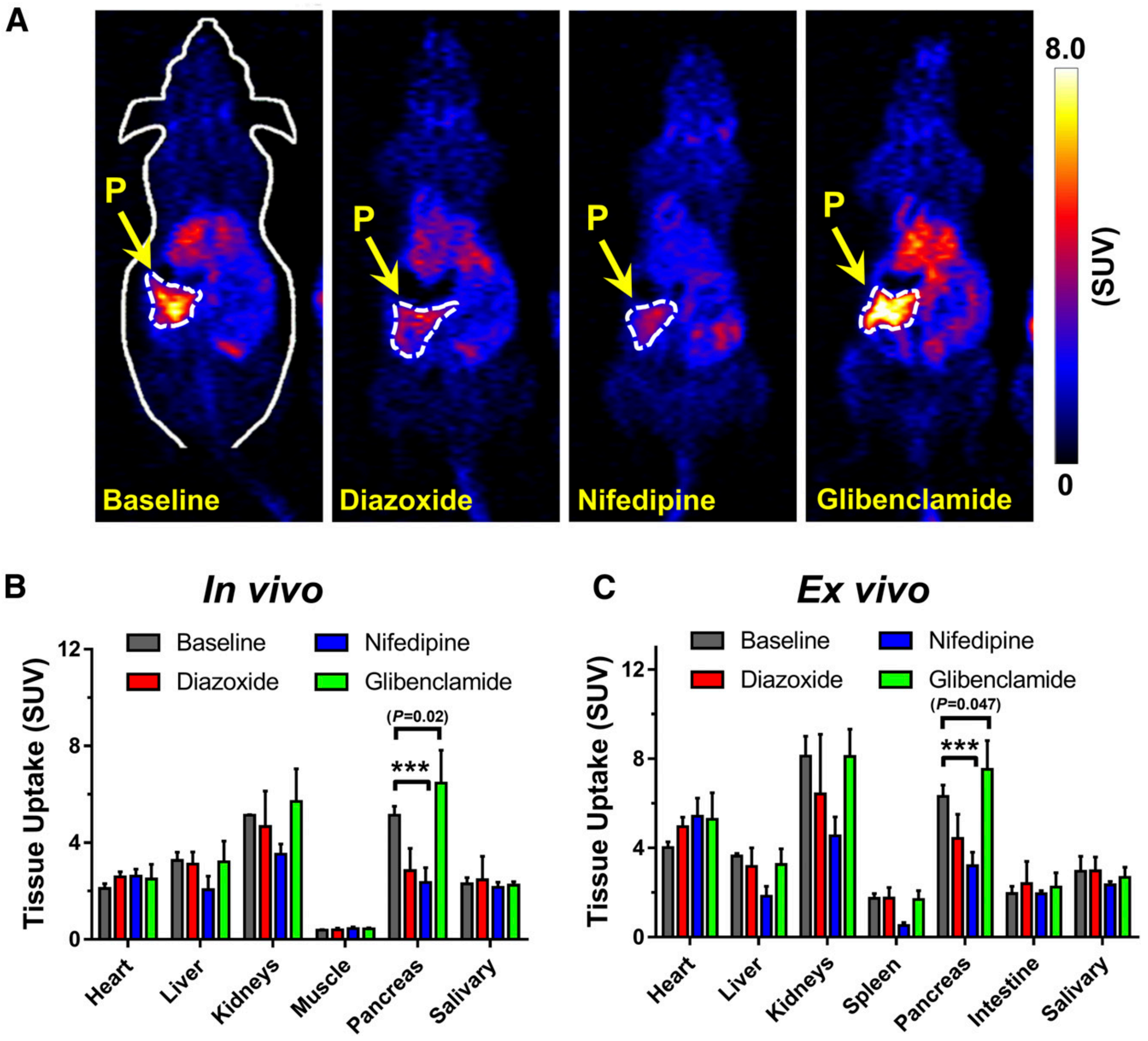

Figure 4—In vivo assessment of functional β-cell mass by $^{52}Mn^{2+}$-PET. *A*: Coronal PET images at 1 h postinjection showing the pancreas of ICR mice given i.p. injections of diazoxide (20 mg/kg), nifedipine (20 mg/kg), or glibenclamide (5 mg/kg) before the administration of a $^{52}Mn^{2+}$ rapid bolus. The pancreas (P) is demarcated by white dashed contours. *B*: Manual ROI-based quantification of $^{52}Mn^{2+}$ uptake in various tissues from static PET images acquired at 1 h postinjection. *C*: Ex vivo biodistribution analysis after PET imaging at 1 h postinjection. Significantly reduced pancreatic uptake of $^{52}Mn^{2+}$ is observed in mice that received nifedipine and diazoxide before radiotracer administration. Mice that received glibenclamide (5 mg/kg) before radiotracer administration had significantly higher pancreatic uptake of $^{52}Mn^{2+}$ than the control mice, based on both PET imaging ($P = 0.02$) and biodistribution ($P = 0.047$) studies. Data are presented as mean ± SD ($n = 3$–4 mice per group). ***$P < 0.001$.

and Supplementary Table 5). Uptake in the liver and salivary gland was very similar in *ob/ob* and wild-type animals, with SUVs of 3.68 ± 0.25 vs. 3.40 ± 0.73 and 3.11 ± 1.05 vs. 2.40 ± 0.20, respectively. In agreement with $^{52}Mn^{2+}$-PET imaging, post hoc analysis of insulin-stained pancreatic sections ($n = 3$) showed a significantly ($P < 0.05$) increased β-cell mass in *ob/ob* mice relative to controls (Fig. 6*C*). We also observed that *ob/ob* islet Ca^{2+} levels, which oscillate in response to glucose stimulation (Fig. 6*D*), were strongly left shifted in their glucose dependence relative to controls (Figs. 6*E* and *F*), in agreement with the in vivo $^{52}Mn^{2+}$-PET results and prior functional studies (22). Notably, in contrast to the experiments in Fig. 4, where pharmacological VDCC manipulation was used to strictly define functional β-cell mass, the experiments in Figs. 5 and 6 show that basal $^{52}Mn^{2+}$ uptake (measured in the absence of exogenous glucose or VDCC inhibitors) remains heavily dependent on changes in β-cell mass. Both approaches, when applied clinically, are likely to yield useful information.

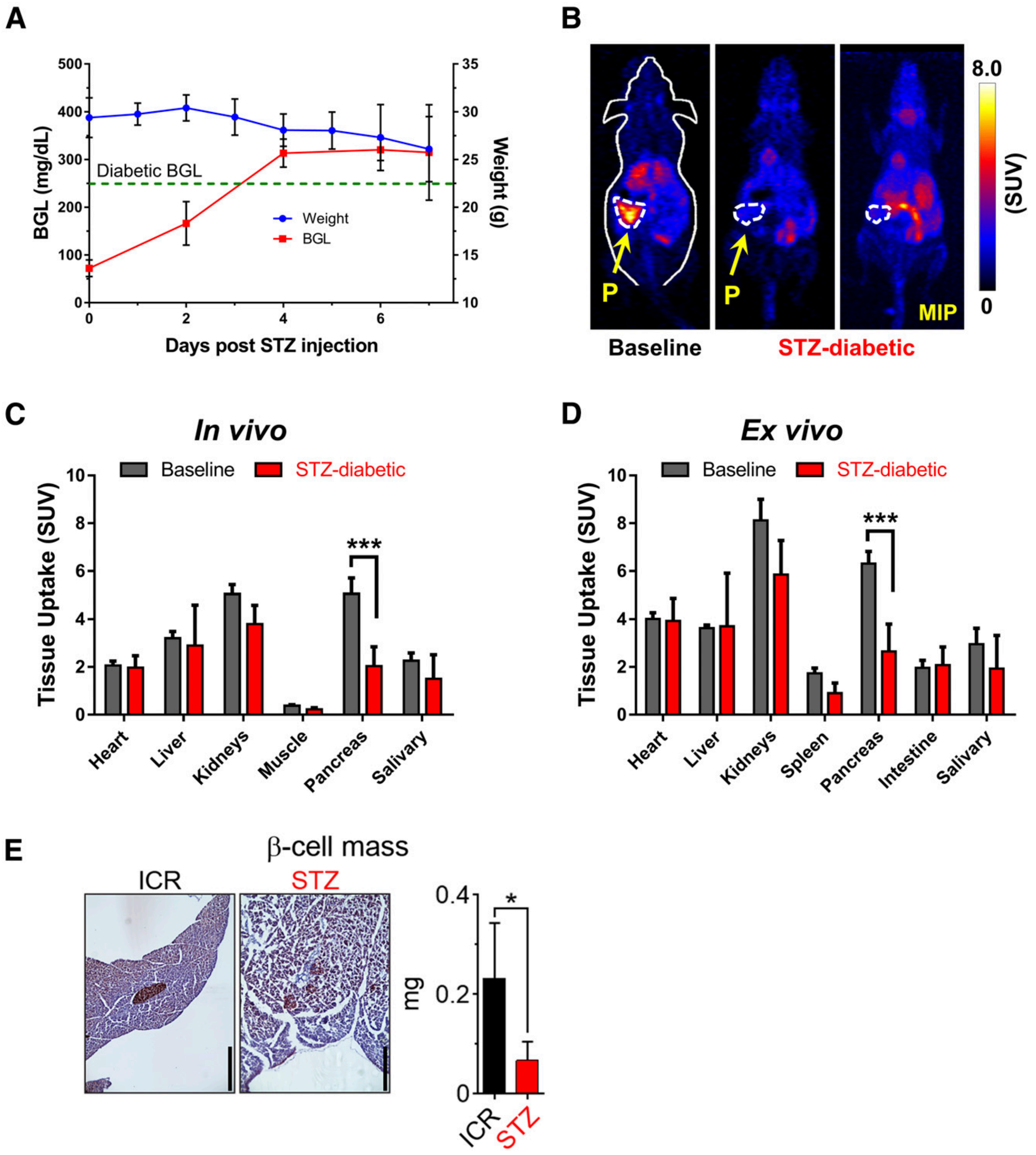

Figure 5—$^{52}Mn^{2+}$-PET imaging in STZ-induced type 1 diabetes. *A*: After the administration of an acute dose of STZ (180 mg/kg), ICR mice started to show symptoms of diabetes: reduced body weight and high blood glucose level (BGL; >250 mg/dL). *B*: At 1 h postinjection, coronal PET images of healthy (left panel) or diabetic (center/right panels) ICR mice show clearly reduced PET signal in the pancreas of the STZ-diabetic mice. The pancreas (P) is demarcated by white dashed contours. The significant decline in $^{52}Mn^{2+}$ uptake in the pancreas of STZ-diabetic mice was confirmed quantitatively by ROI analysis of the PET images (*C*) and ex vivo biodistribution (*D*) (*n* = 3 mice/group). *E*: Quantification of β-cell mass for control and STZ-treated ICR mice. Data are shown as the mean ± SD (*n* = 4 mice/group). Scale bars = 400 μm. $^{*}P < 0.05$, $^{***}P < 0.001$. MIP, maximum intensity projection.

DISCUSSION

The loss of functional β-cell mass is a cornerstone of both type 1 and type 2 diabetes (24). Here, we leveraged the ability of β-cells to sequester divalent metal ions (e.g., Ca^{2+}, Mn^{2+}, Zn^{2+}, and Co^{2+}), which is essential to the production and release of insulin. Although β-cell function has

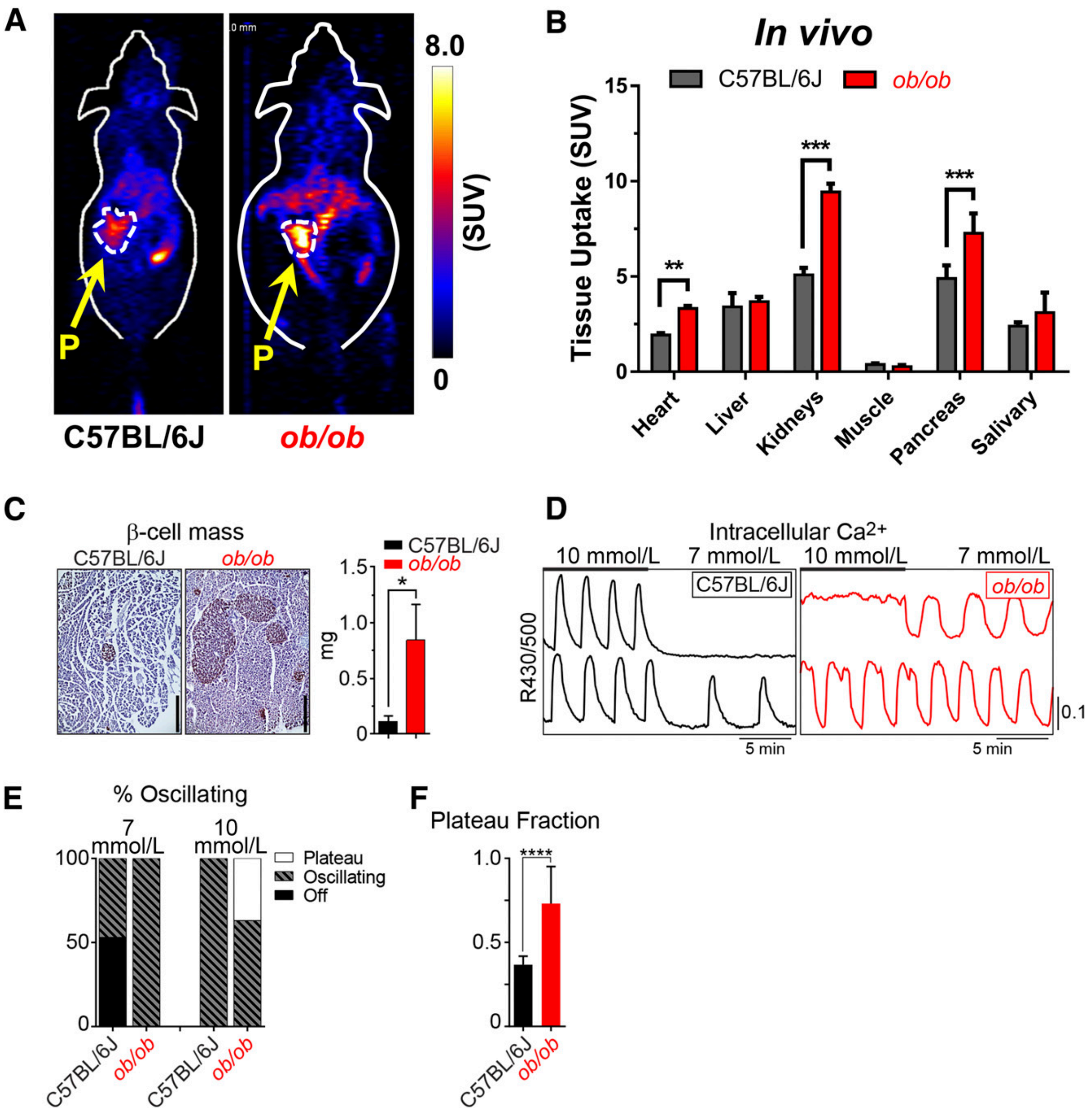

Figure 6—$^{52}Mn^{2+}$-PET imaging in the *ob/ob* model of pretype 2 diabetes. *A*: Coronal PET images acquired at 1 h after $^{52}Mn^{2+}$ administration in *ob/ob* mice and C57BL/6J controls. The pancreas (P) is demarcated by white dashed contours. *B*: Image-derived quantification expressed as SUV indicated a significant difference in $^{52}Mn^{2+}$ pancreatic uptake between groups (mean ± SD; $n = 3$). *C*: Quantification of β-cell mass for wild-type and *ob/ob* mice ($n = 3$ mice/group). Scale bars = 400 μm. *D*: Recordings of islet Ca^{2+} in response to glucose (10 mmol/L and 7 mmol/L) from wild-type and *ob/ob* C57BL/6J mice. *E*: Contingency plot shows the range of islet behaviors at each glucose level. *F*: The oscillatory plateau fraction, reflecting the plasma membrane glucose sensitivity, was calculated as the fraction of time spent in the active state during each oscillation at 10 mmol/L glucose. C57BL/6J, $n = 141$ islets from 4 mice; *ob/ob*, $n = 126$ islets from 4 mice. Results reflect mean ± SD. $^{*}P < 0.05$, $^{**}P < 0.01$, $^{***}P < 0.001$, $^{****}P < 0.0001$.

been widely investigated based on the measurement of Ca^{2+} currents in vitro (25), little progress has been achieved in exploring divalent metal intake for measurement of functional β-cell mass in vivo. Part of this is a result of the lack of effective methods to track the distribution of most of these metals. Fortunately, $^{52}Mn^{2+}$ has both magnetic and nuclear properties that facilitate its noninvasive detection by MRI, and with greater sensitivity, PET. In the present work, we report the use of $^{52}Mn^{2+}$ for noninvasive PET imaging of the mouse pancreas. When injected i.v., $^{52}Mn^{2+}$ accumulated significantly into pancreatic tissue with exceptionally fast blood extraction kinetics. $^{52}Mn^{2+}$ uptake in the pancreas, which peaked within minutes after administration in healthy mice, was on the order of 5–6 SUV, with a slow clearance half-life of ~8 days. Our results demonstrate that in vivo measurements of functional β-cell mass by $^{52}Mn^{2+}$-PET offers complementary information to existing β-cell function assays that lack spatial information (e.g., measurement of c-peptide release), as well as measures of β-cell mass that cannot predict β-cell function (e.g., PET imaging with radiolabeled exendin-4).

A key finding of our work was that 50–60% of the observed pancreatic radioactivity resulted from the specific uptake of $^{52}Mn^{2+}$ through VDCC, implicating β-cells. By pharmacologically manipulating the mechanism of VDCC in isolated islets, we were able to correlate the uptake of radioactive $^{52}Mn^{2+}$ with Ca^{2+} uptake. This agrees with other in vitro studies using nonradioactive Mn^{2+} that reported a correlation between Mn^{2+} uptake and changes in β-cell functional capacity arising from the triggering pathway (14,15,26). Similarly, in vivo studies demonstrated that chemical inhibition of VDCC, using nifedipine or diazoxide, resulted in a drastic decline in the accumulation of $^{52}Mn^{2+}$ within the pancreas. In addition, the stimulation of VDCC with glucose and glibenclamide led to an increase in $^{52}Mn^{2+}$ uptake in the pancreas. Overall, our results indicated that the $^{52}Mn^{2+}$ uptake observed in the pancreas was largely mediated by and dependent on the functional β-cell mass, keeping in mind that $^{52}Mn^{2+}$-PET would be blind to defects in the neurohormonal amplifying pathways of insulin secretion, which are largely VDCC independent (27).

Our next question was whether this method was sensitive enough to detect changes in functional β-cell mass that occur during diabetes progression and disease. First, we used an experimental animal model of STZ-induced type 1 diabetes, which showed an ~60% reduction in the pancreatic accumulation of $^{52}Mn^{2+}$, while uptake in other organs remained unaltered. Direct measurements of β-cell mass by histology showed a comparable decline (~70%), indicating the capability of $^{52}Mn^{2+}$-PET imaging for revealing extreme cases of β-cell loss. Equally relevant results were observed in the obese mouse (*ob/ob*) model of pretype 2 diabetes, where significant ($P < 0.0001$) enhancement in pancreatic uptake of $^{52}Mn^{2+}$ was observed. These results agree with previous reports showing that *ob/ob* mice do not progress to type 2 diabetes (28,29) but rather present markedly higher functional β-cell mass compared with wild-type mice at 10 weeks of age, as assessed by histology and live-cell Ca^{2+} imaging. Probing the gradual gain/loss of functional β-cell mass using $^{52}Mn^{2+}$ ($t_{1/2}$= 5.6 days) was not feasible as a result of its long radioactive half-life. Rather than trying to account for the remnant $^{52}Mn^{2+}$ radioactivity in the pancreas, longitudinal studies would benefit from the use of the shorter-lived $^{51}Mn^{2+}$ ($t_{1/2}$: 45.6 min), which would facilitate regular monitoring of variations in functional β-cell mass without the interference of remnant radioactivity. This is the subject of our future work.

Because significant changes can occur in β-cell function long before changes in anatomical mass are observed (30–32), it is advantageous that the relative uptake of $^{52/51}Mn^{2+}$ in vivo depends on the functional β-cell mass. This ability has the potential to shed light on the rate of functional β-cell mass decline in asymptomatic patients with type 1 diabetes as well as the survival of β-cell transplants, including stem cell–derived β-cells. Whether $^{51/52}Mn^{2+}$-PET is capable of measuring very subtle changes in this parameter is the pivotal question to its clinical significance. The diffusion of Mn^{2+} through β-cell VDCCs depends on their activation by glucose or drug-based stimulation. This has been shown here through in vitro and in vivo functional suppression and enhancement studies. For a given state of glucose activation, the amount of Mn^{2+} cellular internalization by the pancreas is partly controlled by the number of available VDCCs, which should be proportional to functional β-cell mass. However, accurate quantification of functional β-cell mass will require subtraction of nonspecific exocrine pancreas uptake of the radiotracer. For this reason, the $^{52}Mn^{2+}$-PET measurements in *ob/ob* mice underestimate the predicted effect on functional β-cell mass. Calibration may be accomplished through pharmacological manipulation to acutely suppress VDCC-mediated uptake of $^{52}Mn^{2+}$ using nifedipine, diazoxide, or other suppressing agents. However, same-subject calibration will require the implementation of back-to-back PET scans using the shorter-lived $^{51}Mn^{2+}$ or the performance of dynamic PET scanning under a $^{52}Mn^{2+}$ infusion regimen that allows for the deconvolution of the endocrine signal from the exocrine background.

Aside from VDCC, there are several endogenous mechanisms for Mn^{2+} uptake, including facilitated diffusion, divalent metal transporter-1 (DMT1), Zrt- and Irt-related protein-8 (ZIP-8), transferrin receptor (TfR), and ionotropic glutamate receptor Ca^{2+} channels (8). The relative role that these alternative pathways play in $^{52}Mn^{2+}$ transport remains unknown, but a lack of effect by nifedipine suggests that VDCC may not be a primary transport route in many normal tissues. In this regard, our studies also provided valuable information on the kinetics of the whole-body distribution of $^{52}Mn^{2+}$. Besides the pancreas, $^{52}Mn^{2+}$ also accumulated in the liver, heart, kidneys, and salivary gland. No clear sign of renal excretion was observed despite the significant kidney uptake, and most of the $^{52}Mn^{2+}$ clearance occurred through the hepatobiliary system. From the analysis of the image-derived dynamic TAC of the heart, we estimated a $^{52}Mn^{2+}$ circulation half-life of 10.7 ± 3.5 s after a rapid bolus i.v. injection, which aligned with previous studies showing an extremely fast (~0.8 min) blood clearance of ^{54}Mn in dogs (33). Such fast extraction kinetics indicate that compartmental modeling could be used to describe $^{52}Mn^{2+}$ uptake in a more quantitative manner. A stable residual myocardial uptake was observed after complete blood clearance, ~1 min after injection. Of note was the marked underestimation of myocardial uptake by PET compared with biodistribution results, with an average recovery coefficient of 0.54. This is an inherent limitation of the PET imaging–based quantification of small volumes such as the myocardial wall or adrenal glands, which in mice are affected by significant partial volume effects (34,35).

Several PET tracers have been studied as potential β-cell imaging agents. [^{11}C]-dihydrotetrabenazine (DTBZ) and the ^{18}F-labeled DTBZ analog FP-(+)-DTBZ have been shown to have high affinity for the type 2 vesicular acetylcholine transporter (VMAT2), which is expressed on the surface of rodent β-cells but appears to be entirely absent from pancreatic exocrine tissue (36–39). Unfortunately, primate models have shown very low pancreatic uptake of [^{11}C]-DTBZ, which suggests that the degree of VMAT2 expression is species dependent (40–42). More work is needed in quantifying human β-cell expression of VMAT2 and how expression density is related to β-cell function. Another promising PET approach for monitoring in vivo β-cell mass involves compartmental kinetic analysis of [^{11}C]5-hydroxytryptophan (HTP), a compound used clinically for detection of neuroendocrine tumors (43). This compound has shown differential clearance from endocrine versus exocrine pancreatic tissues based on differences in the presence of serotonin biosynthesis machinery, which effect [^{11}C]5-HTP retention in endocrine cells. With this approach, [^{11}C]5-HTP tracer uptake is observed to decrease both longitudinally in patients with type 2 diabetes and cross-sectionally in patients with type 1 diabetes compared with healthy control subjects (44,45). Another category of tracers includes radiolabeled (e.g., ^{18}F, ^{68}Ga, ^{64}Cu, ^{111}In) derivatives of exendin-4, a glucagon-like protein-1 receptor agonist (46–50). Fluorescence microscopy has shown that glucagon-like protein-1 receptor is only located on β-cells within the human pancreas (51), making it an attractive molecular imaging target as a result of its specificity. In animal models, exendin-4–PET suffers from low pancreatic uptake relative to the surrounding organs ($<$0.3%ID/g in Sprague-Dawley rats at 1 h postinjection, whereas proximal kidney uptake is $>$25%ID/g) (52). Although the kidney uptake of $^{52}Mn^{2+}$ is also significant, the pancreatic uptake of $^{52}Mn^{2+}$ is comparatively high, such that improved pancreas-to-background ratios are attained by $^{52}Mn^{2+}$-PET. In general, the implementation of tracers targeting surface receptors of β-cells is extremely challenging, considering the low total mass of β-cells, diffuse pancreatic distribution, and heterogeneous receptor expression.

Aside from following the gain/loss of β-cell mass in patients with prediabetes/diabetes, there is a pressing need for a noninvasive method for longitudinal imaging of β-cell transplants. Islet transplantation has been shown to lead to temporary insulin independence in patients with type 1 diabetes (53,54) but has not been widely adopted because of the need for donor tissues. Recent advances in selective stem cell differentiation techniques will likely lead to wider clinical adoption of β-cell transplantation therapies (55). The ability to noninvasively track the survival and function of transplanted β-cells would enable research into the patient-specific efficacy assessment of immune-modulating therapies and the development of new therapeutic strategies (56). In this case, the use of $^{51}Mn^{2+}$-PET for monitoring islet transplant survival is compelling because it can be performed repeatedly and safely over time.

In conclusion, the prominent pancreatic uptake, rapid localization kinetics, and well-characterized metabolic pathways of $^{52}Mn^{2+}$ make it a promising agent for noninvasive PET imaging of functional β-cell mass and was corroborated by various post hoc experiments such as histological β-cell mass measurements and live-cell imaging of β-cell Ca^{2+} oscillations. With further development, $^{51}Mn^{2+}$-PET may also find broad applications in venues ranging from basic research to clinical patient care.

Acknowledgments. The authors are grateful to Dr. James Holden (Department of Medical Physics, University of Wisconsin) for sharing his expertise in the experimental design and dynamic PET modeling.

Funding. The laboratory of M.J.M. received support from the American Diabetes Association (1-16-IBS-212, 1-17-PDF-155), the National Institutes of Health (NIH)/National Institute of Diabetes and Digestive and Kidney Diseases (K01-DK-01683), the NIH/National Institute of Aging (R21-AG-050135), and the University of Wisconsin-Madison School of Medicine and Public Health Wisconsin Partnership Program. The laboratory of W.C. received support from the University of Wisconsin-Madison, the National Science Foundation Division of Graduate Education (DGE-1256259), NIH (T32-CA-009206), the National Institute of Biomedical Imaging and Bioengineering (1R01-EB-021336), National Cancer Institute (1R01-CA-169365, P30-CA-014520), and National Institute of General Medical Sciences (T32-GM-008349).

Duality of Interest. No potential conflicts of interest relevant to this article were reported.

Author Contributions. R.H. and S.A.G. conceived the project, performed preparatory experimentation and method development, collected and analyzed data, and prepared the manuscript. T.G. contributed to the experimental design and assisted with the ex vivo $^{52}Mn^{2+}$-PET experiments. H.R.V. performed the Ca^{2+} imaging studies. R.J.F. and H.N.W. performed the β-cell mass measurements. C.G.E. and J.J.J. assisted with PET image acquisition, ex vivo biodistribution studies, and data analysis. H.F.V., T.E.B., and G.W.S. developed radioisotope production tools, assisted with tracer quality assurance, and contributed to experimental design. R.J.N., M.E.K., M.J.M., and W.C. supervised project execution, provided technical support, assisted with data interpretation, and edited the manuscript. M.J.M. and W.C. are the guarantors of this work and, as such, had full access to all the data in the study and take responsibility for the integrity of the data and the accuracy of the data analysis.

Prior Presentation. Parts of this study were presented in abstract form at the 63rd Annual Meeting of the Society of Nuclear Medicine and Molecular Imaging, San Diego, CA, 1–15 June 2016, and the 58th Annual Meeting of the American Association of Physicists in Medicine, Washington, DC, 31 July–4 August 2016.

References

1. Forbes JM, Cooper ME. Mechanisms of diabetic complications. Physiol Rev 2013;93:137–188
2. Ionescu-Tirgoviste C, Gagniuc PA, Gubceac E, et al. A 3D map of the islet routes throughout the healthy human pancreas. Sci Rep 2015;5:14634
3. Kim A, Miller K, Jo J, Kilimnik G, Wojcik P, Hara M. Islet architecture: a comparative study. Islets 2009;1:129–136
4. von Mach MA, Schlosser J, Weiland M, et al. Size of pancreatic islets of Langerhans: a key parameter for viability after cryopreservation. Acta Diabetol 2003;40:123–129
5. Kilimnik G, Jo J, Periwal V, Zielinski MC, Hara M. Quantification of islet size and architecture. Islets 2012;4:167–172
6. Virostko J, Powers AC. Molecular imaging of the pancreas in small animal models. Gastroenterology 2009;136:407–409

7. Paulus MJ, Gleason SS, Easterly ME, Foltz CJ. A review of high-resolution X-ray computed tomography and other imaging modalities for small animal research. Lab Anim (NY) 2001;30:36–45

8. Au C, Benedetto A, Aschner M. Manganese transport in eukaryotes: the role of DMT1. Neurotoxicology 2008;29:569–576

9. Silva AC, Lee JH, Aoki I, Koretsky AP. Manganese-enhanced magnetic resonance imaging (MEMRI): methodological and practical considerations. NMR Biomed 2004;17:532–543

10. Antkowiak PF, Stevens BK, Nunemaker CS, McDuffie M, Epstein FH. Manganese-enhanced magnetic resonance imaging detects declining pancreatic β-cell mass in a cyclophosphamide-accelerated mouse model of type 1 diabetes. Diabetes 2013;62:44–48

11. Antkowiak PF, Tersey SA, Carter JD, et al. Noninvasive assessment of pancreatic beta-cell function in vivo with manganese-enhanced magnetic resonance imaging. Am J Physiol Endocrinol Metab 2009;296:E573–E578

12. Antkowiak PF, Vandsburger MH, Epstein FH. Quantitative pancreatic β cell MRI using manganese-enhanced Look-Locker imaging and two-site water exchange analysis. Magn Reson Med 2012;67:1730–1739

13. Lamprianou S, Immonen R, Nabuurs C, et al. High-resolution magnetic resonance imaging quantitatively detects individual pancreatic islets. Diabetes 2011;60:2853–2860

14. Rorsman P, Berggren PO, Hellman B. Manganese accumulation in pancreatic beta-cells and its stimulation by glucose. Biochem J 1982;202:435–444

15. Rorsman P, Hellman B. The interaction between manganese and calcium fluxes in pancreatic β-cells. Biochem J 1983;210:307–314

16. Crossgrove J, Zheng W. Manganese toxicity upon overexposure. NMR Biomed 2004;17:544–553

17. Lenzen S. The mechanisms of alloxan- and streptozotocin-induced diabetes. Diabetologia 2008;51:216–226

18. Tanaka K, Kawano T, Tomino T, et al. Mechanisms of impaired glucose tolerance and insulin secretion during isoflurane anesthesia. Anesthesiology 2009;111:1044–1051

19. Desborough JP, Jones PM, Persaud SJ, Landon MJ, Howell SL. Isoflurane inhibits insulin secretion from isolated rat pancreatic islets of Langerhans. Br J Anaesth 1993;71:873–876

20. Lucaciu CM, Dragu C, Copăescu L, Morariu VV. Manganese transport through human erythrocyte membranes. An EPR study. Biochim Biophys Acta 1997;1328:90–98

21. Shibuya I, Douglas WW. Calcium channels in rat melanotrophs are permeable to manganese, cobalt, cadmium, and lanthanum, but not to nickel: evidence provided by fluorescence changes in fura-2-loaded cells. Endocrinology 1992;131:1936–1941

22. Irles E, Ñeco P, Lluesma M, et al. Enhanced glucose-induced intracellular signaling promotes insulin hypersecretion: pancreatic beta-cell functional adaptations in a model of genetic obesity and prediabetes. Mol Cell Endocrinol 2015;404:46–55

23. Merrins MJ, Poudel C, McKenna JP, et al. Phase analysis of metabolic oscillations and membrane potential in pancreatic islet β-cells. Biophys J 2016;110:691–699

24. Weir GC, Bonner-Weir S. Five stages of evolving beta-cell dysfunction during progression to diabetes. Diabetes 2004;53(Suppl. 3):S16–S21

25. Atwater I, Dawson CM, Scott A, Eddlestone G, Rojas E. The nature of the oscillatory behaviour in electrical activity from pancreatic beta-cell. Horm Metab Res Suppl 1980;Suppl. 10:100–107

26. Gimi B, Leoni L, Oberholzer J, et al. Functional MR microimaging of pancreatic beta-cell activation. Cell Transplant 2006;15:195–203

27. Prentki M, Matschinsky FM, Madiraju SR. Metabolic signaling in fuel-induced insulin secretion. Cell Metab 2013;18:162–185

28. Bock T, Pakkenberg B, Buschard K. Increased islet volume but unchanged islet number in ob/ob mice. Diabetes 2003;52:1716–1722

29. Golson ML, Misfeldt AA, Kopsombut UG, Petersen CP, Gannon M. High fat diet regulation of β-cell proliferation and β-cell mass. Open Endocrinol J 2010;4:66–77

30. Ha J, Satin LS, Sherman AS. A mathematical model of the pathogenesis, prevention, and reversal of type 2 diabetes. Endocrinology 2016;157:624–635

31. Couri CE, Oliveira MC, Stracieri AB, et al. C-peptide levels and insulin independence following autologous nonmyeloablative hematopoietic stem cell transplantation in newly diagnosed type 1 diabetes mellitus. JAMA 2009;301:1573–1579

32. Voltarelli JC, Couri CE, Stracieri AB, et al. Autologous nonmyeloablative hematopoietic stem cell transplantation in newly diagnosed type 1 diabetes mellitus. JAMA 2007;297:1568–1576

33. Atkins HL, Som P, Fairchild RG, et al. Myocardial positron tomography with manganese-52m. Radiology 1979;133:769–774

34. Erlandsson K, Buvat I, Pretorius PH, Thomas BA, Hutton BF. A review of partial volume correction techniques for emission tomography and their applications in neurology, cardiology and oncology. Phys Med Biol 2012;57:R119–R159

35. Gargiulo S, Greco A, Gramanzini M, et al. PET/CT imaging in mouse models of myocardial ischemia. J Biomed Biotechnol 2012;2012:541872

36. Eriksson O, Jahan M, Johnström P, et al. In vivo and in vitro characterization of [18F]-FE-(+)-DTBZ as a tracer for beta-cell mass. Nucl Med Biol 2010;37:357–363

37. Kung MP, Hou C, Lieberman BP, et al. In vivo imaging of β-cell mass in rats using ^{18}F-FP-(+)-DTBZ: a potential PET ligand for studying diabetes mellitus. J Nucl Med 2008;49:1171–1176

38. Simpson NR, Souza F, Witkowski P, et al. Visualizing pancreatic β-cell mass with [11C]DTBZ. Nucl Med Biol 2006;33:855–864

39. Singhal T, Ding YS, Weinzimmer D, et al. Pancreatic beta cell mass PET imaging and quantification with [^{11}C]DTBZ and [^{18}F]FP-(+)-DTBZ in rodent models of diabetes. Mol Imaging Biol 2011;13:973–984

40. Schäfer MK, Hartwig NR, Kalmbach N, et al. Species-specific vesicular monoamine transporter 2 (VMAT2) expression in mammalian pancreatic beta cells: implications for optimising radioligand-based human beta cell mass (BCM) imaging in animal models. Diabetologia 2013;56:1047–1056

41. Murthy R, Harris P, Simpson N, et al. Whole body [^{11}C]-dihydrotetrabenazine imaging of baboons: biodistribution and human radiation dosimetry estimates. Eur J Nucl Med Mol Imaging 2008;35:790–797

42. Moore A. Advances in beta-cell imaging. Eur J Radiol 2009;70:254–257

43. Di Gialleonardo V, Signore A, Scheerstra EA, et al. ^{11}C-hydroxytryptophan uptake and metabolism in endocrine and exocrine pancreas. J Nucl Med 2012;53:1755–1763

44. Eriksson O, Espes D, Selvaraju RK, et al. Positron emission tomography ligand [^{11}C]5-hydroxy-tryptophan can be used as a surrogate marker for the human endocrine pancreas. Diabetes 2014;63:3428–3437

45. Carlbom L, Espes D, Lubberink M, et al. [$^{(11)}$C]5-hydroxy-tryptophan PET for assessment of islet mass during progression of type 2 diabetes. Diabetes 2017;66:1286–1292

46. Brom M, Woliner-van der Weg W, Joosten L, et al. Non-invasive quantification of the beta cell mass by SPECT with ^{111}In-labelled exendin. Diabetologia 2014;57:950–959

47. Kiesewetter DO, Gao H, Ma Y, et al. ^{18}F-radiolabeled analogs of exendin-4 for PET imaging of GLP-1 in insulinoma. Eur J Nucl Med Mol Imaging 2012;39:463–473

48. Mikkola K, Yim CB, Fagerholm V, et al. ^{64}Cu- and ^{68}Ga-labelled [Nle(14),Lys(40)(Ahx-NODAGA)NH2]-exendin-4 for pancreatic beta cell imaging in rats. Mol Imaging Biol 2014;16:255–263

49. Selvaraju RK, Velikyan I, Johansson L, et al. In vivo imaging of the glucagonlike peptide 1 receptor in the pancreas with ^{68}Ga-labeled DO3A-exendin-4. J Nucl Med 2013;54:1458–1463

50. Wu Z, Todorov I, Li L, et al. In vivo imaging of transplanted islets with ^{64}Cu-DO3A-VS-Cys40-Exendin-4 by targeting GLP-1 receptor. Bioconjug Chem 2011;22:1587–1594

51. Tornehave D, Kristensen P, Rømer J, Knudsen LB, Heller RS. Expression of the GLP-1 receptor in mouse, rat, and human pancreas. J Histochem Cytochem 2008;56:841–851

52. Bandara N, Zheleznyak A, Cherukuri K, et al. Evaluation of Cu-64 and Ga-68 radiolabeled glucagon-like peptide-1 receptor agonists as PET tracers for pancreatic β cell imaging. Mol Imaging Biol 2016;18:90–98

53. Eter WA, Bos D, Frielink C, Boerman OC, Brom M, Gotthardt M. Graft revascularization is essential for non-invasive monitoring of transplanted islets with radiolabeled exendin. Sci Rep 2015;5:15521
54. Paty BW, Bonner-Weir S, Laughlin MR, McEwan AJ, Shapiro AM. Toward development of imaging modalities for islets after transplantation: insights from the National Institutes of Health Workshop on Beta Cell Imaging. Transplantation 2004;77:1133–1137
55. Vegas AJ, Veiseh O, Gürtler M, et al. Long-term glycemic control using polymer-encapsulated human stem cell-derived beta cells in immune-competent mice [published correction appears in Nat Med 2016;22:446] Nat Med 2016;22:306–311
56. Gotthardt M, Eizirik DL, Cnop M, Brom M. Beta cell imaging - a key tool in optimized diabetes prevention and treatment. Trends Endocrinol Metab 2014;25:375–377